Current-phase relations of InAs nanowire Josephson junctions: From interacting to multimode regimes

Sean Hart, Zheng Cui, Gerbold Ménard, Mingtang Deng, Andrey E. Antipov, Roman M. Lutchyn, Peter Krogstrup, Charles M. Marcus, and Kathryn A. Moler

Current-phase relations of InAs nanowire Josephson junctions: from interacting to multi-mode regimes

Sean Hart,[1, 2, *] Zheng Cui,[1, 2, 3, *] Gerbold Ménard,[4] Mingtang Deng,[4] Andrey E. Antipov,[5] Roman M. Lutchyn,[5] Peter Krogstrup,[4, 6] Charles M. Marcus,[4] and Kathryn A. Moler[1, 2, 3]

[1]*Stanford Institute for Materials and Energy Sciences,*
SLAC National Accelerator Laboratory, Menlo Park, California 94025, USA.
[2]*Geballe Laboratory for Advanced Materials, Stanford University, Stanford, California 94305, USA.*
[3]*Department of Applied Physics, Stanford University, Stanford, California 94305, USA.*
[4]*Center for Quantum Devices and Microsoft Quantum Lab - Copenhagen,*
Niels Bohr Institute, University of Copenhagen, Copenhagen DK-2100, Denmark.
[5]*Station Q, Microsoft Research, Santa Barbara, California 93106-6105, USA.*
[6]*Microsoft Quantum Materials Lab, Copenhagen, Denmark.*

Gate-tunable semiconductor-superconductor nanowires with superconducting leads form exotic Josephson junctions that are a highly desirable platform for two types of qubits: those with topological superconductivity (Majorana qubits) and those based on tunable anharmonicity (gatemon qubits). Controlling their behavior, however, requires understanding their electrostatic environment and electronic structure. Here we study gated InAs nanowires with epitaxial aluminum shells. By measuring current-phase relations (CPR) and comparing them with analytical and numerical calculations, we show that we can tune the number of modes, determine the transparency of each mode, and tune into regimes in which electron-electron interactions are apparent, indicating the presence of a quantum dot. To take into account electrostatic and geometrical effects, we perform microscopic self-consistent Schrodinger-Poisson numerical simulations, revealing the energy spectrum of Andreev states in the junction as well as their spatial distribution. Our work systematically demonstrates the effect of device geometry, gate voltage and phase bias on mode behavior, providing new insights into ongoing experimental efforts and predictive device design.

INTRODUCTION

Studies of hybrid structures of superconductors and semiconducting nanowires have recently spurred advances in fundamental physics, materials science, and technology [1]. A growing body of experimental evidence supports proposals that nanowire-superconductor hybrids can host Majorana modes, the building blocks in schemes for topological quantum computing [2–13]. Gate-tunable nanowire Josephson junctions have also been integrated into a cavity-QED architecture, providing electrostatic control of the qubit transition frequency [14, 15]. Improving the design and operation of these devices will rely on understanding their electrostatic environment and electronic structure, with several recent works examining mode behavior in wire devices [16–21]. Moreover, electron-electron interactions, often overlooked in both experiment and theory, should also be considered as they are expected to play an important role, particularly in one or fewer dimensions.

Here we report measurements of the current-phase relation (CPR) of a Josephson junction based on an InAs nanowire, carried out using a scanning Superconducting QUantum Interference Device (SQUID) microscope. The amplitude and phase dependence of the CPR are sensitive to the transparency and number of modes contributing to supercurrent in the junction[17, 22–25]. Micro-

scopic regimes with one or multiple modes can be distinguished through comparison to a simple analytic model, by a model-independent analysis, and by comparison to numerical simulations. The qualitative agreement of the current-phase relations between our simulations and experiment enables the use of numerical modeling for visualizing the microscopic effect of electrostatic gating. In the regime of low electron density in the junction, we find evidence for interactions, which modify both the spectrum and the phase-dependence of current flow in the device (i.e., lead to a sign reversal of the supercurrent). Our simulation of the device behavior, combined with our understanding and control of both interactions and anharmonicity, provides new insight into recent experiments and allows for more deterministic device design.

MEASURING THE CURRENT-PHASE RELATION OF AN INAS NANOWIRE JOSEPHSON JUNCTION

To investigate the CPR of the InAs nanowire Josephson junction, we fabricated a superconducting ring consisting of a 100 nm thick annular film of evaporated aluminum bridged by a hybrid epitaxial aluminum-InAs nanowire (figure 1a). The Josephson junction is located at the center of the nanowire. To measure the current-phase relation, we positioned the pickup loop and field coil of a SQUID microscope approximately 1 micron above the sample ring [26]. When a current is applied to the field coil, a magnetic flux Φ is generated in the
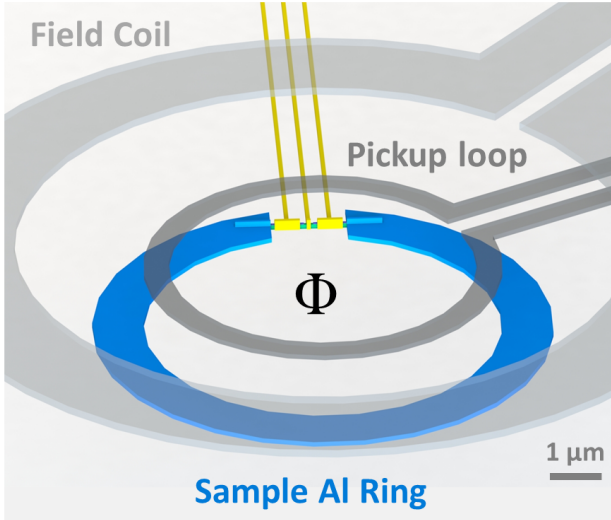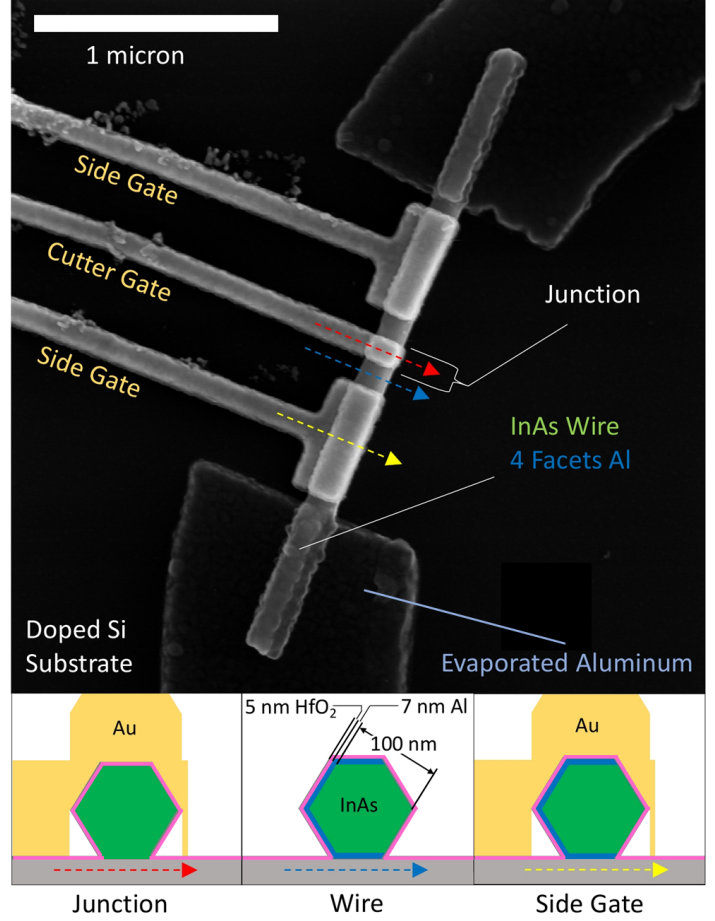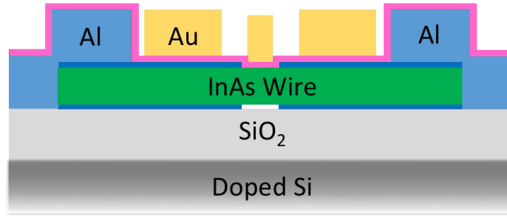
---

a. Current-Phase Relation measurement setup

b. Locally gated InAs Josephson junction

c. Junction side cross-section

FIG. 1. Experimental setup to measure the current-phase relation of an InAs nanowire-based Josephson junction. a) The sample ring consists of an evaporated aluminum ring (blue), which is interrupted by an InAs nanowire (green with yellow gates) to form a Josephson junction. To measure the current-phase relation of the junction, the sensing head of a SQUID microscope is positioned above the sample ring. A current bias applied to the field coil (light grey) tunes the magnetic flux through the sample ring, providing control of the phase difference across the junction. This phase difference determines the supercurrent in the junction via its current-phase relation. The supercurrent circulates in the sample ring, leading to a signal which is measured by the pickup loop (dark grey). Drawing is to scale. b) A scanning electron micrograph depicts a top view of the portion of the sample ring spanned by the InAs nanowire. As depicted in the bottom panels, the nanowire has a hexagonal cross-section, and is coated epitaxially on four facets with a 7 nm layer of aluminum (blue). This epitaxial aluminum layer is chemically removed along a 100 nm span beneath the cutter gate, while the wire is isolated from the gate with a 5 nm layer of HfO$_2$ (pink), shown in bottom left cross-section. The center and right cross-sections indicate the structure of the wire in ungated sections and in sections with a side gate. The respective locations of the cross-sections are labeled by red, blue and yellow arrows on the SEM image. c) A cross-sectional side view of the wire shows the layer structure of the device. The sample ring rests on a doped silicon substrate, providing the ability to gate the device globally from below.

sample ring. This flux directly tunes the phase difference ϕ across the nanowire junction, leading to a supercurrent in the junction due to its current-phase relation. The supercurrent circulates in the sample ring and is measured as a flux in the pickup loop [23, 24, 27]. The center position of the ring can be found with sub-micron precision by the diamagnetic response from the ring. By modeling the SQUID-sample geometry and calibrating the mutual inductance against the periodicity of the current-phase

relation, we convert the flux signal into a Josephson supercurrent in the ring [28]. The mutual inductance can change up to 5% over long periods of time due to drift in the SQUID position. Since we calibrate the mutual inductance for each CPR measurement, our analysis is not affected by this drift.

The hybrid nanowires are grown by Molecular Beam Epitaxy [29]. Au-catalyzed InAs nanowires are first grown via the vapor-liquid-solid method followed by a

low temperature in-situ growth step of 7 nm aluminum on four of the six side facets (figure 1b). The four facet coverage is realized in two steps of two-facet growth with an intermediate 120 degree rotation of the nanowire orientation with respect to the atomic aluminum beam, which ensures a flat continuous aluminum film on all four facets. This epitaxial aluminum makes electrical contact with the evaporated aluminum film to close the ring. In the center of the nanowire, the epitaxial aluminum is chemically removed over a span of 100-150 nm to form the junction. The junction lies under a Ti/Au "cutter" gate, while two additional side gates overlap the wire in regions still contacted with epitaxial aluminum (see figure 1c). A 5 nm layer of HfO_2 (shown in pink) isolates the gates and the wire. The side gates are expected to be mostly screened by aluminum, but can still affect the wire via fringe electric fields. Finally, the sample ring sits on a doped silicon substrate capped with a thin layer of oxide, allowing the wire to be gated from below. We found that the cutter gate and back gate have qualitatively similar effects, indicating that both gates primarily affect the same junction region (under the cutter gate) due to screening from the epitaxial aluminum [28]. Hence, we focus mainly on the modulation of the CPR by the cutter gate and side gates.

MODEL-INDEPENDENT ANALYSIS OF CURRENT-PHASE RELATION VS. CUTTER GATE VOLTAGE

To explore the effect of local gating on the nanowire junction, we measured the CPR at a series of voltages V_C applied to the cutter gate (figure 2a). As the cutter gate voltage is tuned from -2 to 0 V, the amplitude of the CPR evolves through several qualitatively distinct regimes. At the most negative gate voltages, the onset of supercurrent gives way to a set of recurring peaks in the critical current (plotted in black in figure 2b). As the gate voltage increases above $V_C \approx -1.16$ V, the critical current begins to fluctuate with gate voltage. Finally, above $V_C \approx -0.45$ V, the fluctuations diminish and the critical current begins to increase more steeply with gate voltage.

These gate-dependent features of the junction's critical current are accompanied by strong variations in the phase dependence, or shape, of the CPR (visible in figure 2a). The most prominent feature of these shape variations is their forward skew, meaning that the critical current occurs at an advanced phase compared to a sine wave. The skew of a CPR can be characterized by taking its Fourier transform and defining a quantity $S = -A_2/A_1$, where A_1 and A_2 are the first and second harmonics of the CPR. Positive S indicates forward skew, and hereafter we use S and 'skew' interchangeably.

Plotting the skew on the same gate voltage axis as the critical current reveals an intricate interplay between the shape of the CPR and its amplitude (light blue in figure 2b). At the most negative gate voltages, recurring peaks in the critical current are accompanied by coincident peaks in the skew. In the intermediate regime of fluctuating critical current, the skew also fluctuates and some correlations are observable between critical current and skew. As the critical current begins to increase sharply at the most positive gate voltages, the skew remains relatively constant near $S = 0.3$. Throughout the gate trace, it is remarkable that the CPR is almost always forward-skewed ($S > 0$), in sharp contrast with the sinusoidal behavior ($S = 0$) found in the conventional Josephson effect. At certain gate voltages, the skew is not calculated due to the CPR amplitude being too small to obtain a reliable result.

Figure 2d more clearly distinguishes different regimes mentioned above. For $V_C < -1.16$ V, the CPR shows highly correlated amplitude and skew (red dots), distinct from $V_C > -1.16$ V. Next, by comparing the relationship between amplitude and skew to a well-known theoretical model, we quantitatively identify these distinct regimes as having different numbers of supercurrent carrying modes.

SHORT JUNCTION THEORY REVEAL MODE NUMBER AND TRANSPARENCY

The variations of the CPR amplitude and shape with gate voltage contain considerable information about the electronic structure of the junction. The CPR depends on the electronic properties of the junction according to the fundamental relation

$$I(\phi) = \frac{2e}{\hbar} \frac{dF}{d\phi}, \qquad (1)$$

where F is the free energy and ϕ is the phase difference across the Josephson junction [30]. In the limit where the junction length is short compared to the superconducting coherence length, the dominant contribution to the supercurrent comes from discrete spectrum of bound states in the junction, with energies $\epsilon_p = \Delta\sqrt{1 - \tau_p \sin^2(\phi/2)}$ [25]. The energies ϵ_p of these states, called Andreev bound states, are related to the transmission probabilities τ_p of the underlying normal conduction channels in the junction. Here Δ is the amplitude of the Andreev states, and in the short-junction limit is equal to the superconducting gap. With this spectrum, Eq. (1) can be simplified to a well-known formula [31–33]:

a. Cutter gate dependence of CPR

b. Evolution of critical current and skewness vs. cutter gate

c. Perfect transmission single channel

d. CPR amplitude vs. skew

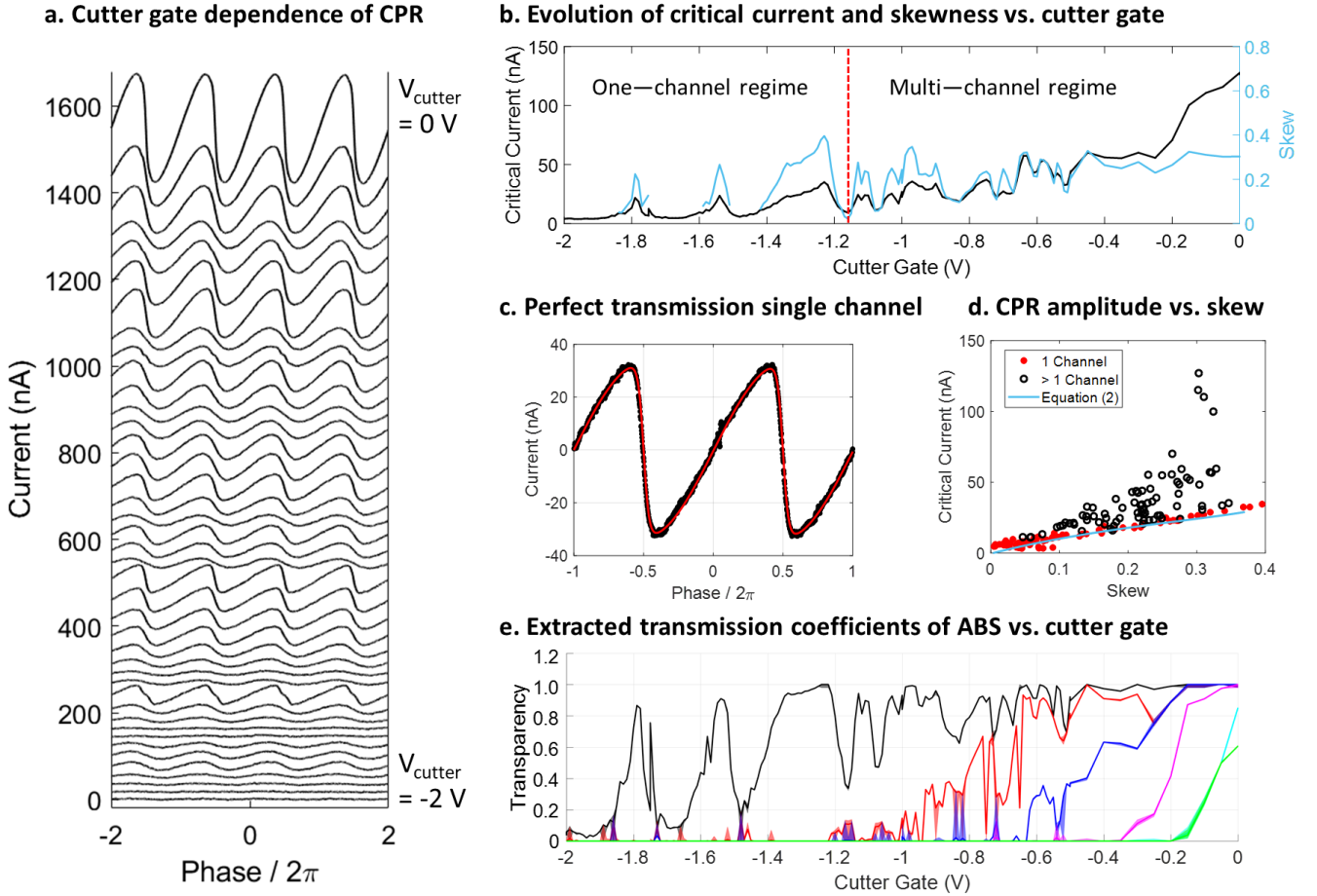**e. Extracted transmission coefficients of ABS vs. cutter gate**

FIG. 2. CPR measurements probe the evolution of supercurrent-carrying modes with gate voltage. a) The amplitude and shape of the CPR evolve as the voltage applied to the cutter gate decreases from 0 to -2 volts, corresponding to changes in the structure of the Andreev bound states as a function of applied electric field. Each curve is a measured current-phase relation at a particular cutter gate voltage. The waterfall plot represents an evenly-spaced subset of the gate sweep, and are offset vertically for clarity. b) The dependence of CPR amplitude and shape on cutter gate voltage. The black curve shows the critical current amplitude (left y-axis) vs. gate voltage. The light blue curve shows CPR skew vs. gate voltage (right y-axis). The skew is calculated as the ratio between the second and first harmonic (i.e. Fourier component) of the CPR, $S = -\frac{A_2}{A_1}$. Recurring peaks at $V_C < -1.16V$ (red dashed line) signified resonant-tunneling in the single-channel regime. c) Fitting CPR data at $V_C = -1.22$ V (black dots) to Eq. 2 (red line) results in a single channel with $\tau = 1$, $T = 98$ mK and $\Delta = 128$ μeV. d) Scatter plot of CPR amplitude vs. skew for all measured cutter gate voltages between 0 V and -2 V reveals distinct regimes. Red dots are taken from $V_C < -1.16$ V, showing highly correlated amplitude and skew expected from a single-channel. Blue curve is the expected single-channel behavior calculated from Eq. 2 (with $T = 98$ mK and $\Delta = 128$ μeV). e) Extracted transmission coefficients $\{\tau_1...\tau_6\}$ from best fits to Eq. 2, showing the evolution of the number and transparency of supercurrent-carrying channels with cutter gate voltage. Different colors are for visual clarity only and are not meant to differentiate physical states. The vertical width of shaded regions represents 68% confidence interval of the fitted parameters.

$$I(\phi) = -\frac{2e}{\hbar} \sum_{p=1}^{N} \frac{d\epsilon_p}{d\phi} \tanh\left(\frac{\epsilon_p}{2k_B T}\right) = \frac{e\Delta^2}{2\hbar} \sin\phi \sum_{p=1}^{N} \frac{\tau_p}{\epsilon_p} \tanh\left(\frac{\epsilon_p}{2k_B T}\right). \tag{2}$$

Here N corresponds to the number of Andreev bound states in the junction.

This simplified model illustrates that the CPR is a sensitive probe of both the number of modes and their trans-

parencies (τ_p). In the simplest case of a single channel, the amplitude and skew of the CPR both increase with τ_1. In a state with low transparency ($\tau_1 \ll 1$), a sinusoidal CPR is expected ($S \to 0$). In a state with high trans-

parency ($\tau_1 \sim 1$), the CPR is forward-skewed ($S > 0$), up to the limit of $S = 0.4$ for $T = 0$ K and $\tau_1 = 1$. When more than one channel contributes to the CPR, the shape and amplitude of the CPR become sensitive to a set of $N > 1$ transmission probabilities.

First we performed fits to Eq. 2 with a highly forward-skewed CPR at $V_C = -1.22$ V, with free parameters $\{\Delta, T, \tau_1, \tau_2, ...\}$. The best fit result is shown in figure 2c, with $\Delta = 128$ μeV, T = 98 mK, $\tau_1 = 1$ and $\tau_p = 0$ for $p > 1$ [28]. The nominal sample stage temperature is ~ 60 mK. Although the fitted effective temperature is slightly elevated, we are still in the regime of $T \ll T_c$ and thus should be free from any noise-induced quasiparticle excitation that could affect the CPR. All wires connected to both the sample and the scanning SQUID are filtered by RF filters with at least 45 dB attenuation above 10 MHz [34]. The extracted amplitude parameter $\Delta = 128$ μeV is the energy of Andreev states at zero phase bias. The comparison between this value and the proximity-induced gap reported in normal-superconducting transport experiments for similar epitaxial-Al covered InAs nanowires [12] is presented in the discussion. Systematic experimental uncertainty is also considered in [28].

We subsequently performed fits of Eq. 2 to the CPR data (with $\Delta = 128$ μeV and T = 98 mK held constant), allowing up to $N = 6$ contributing modes. The best fit result is summarized in figure 2e. Below $V_C \approx -1.16$ V, the CPR is well-described by a single contributing channel. This perfectly coincides with the single-channel regime identified by our model-independent analysis earlier (in figure 2b and d).

Throughout the regime of fluctuating critical current, $V_C \approx -1.16$ V to $V_C \approx -0.45$ V, a second and third channel can be seen to contribute (figure 2e red and blue). Although their respective transparencies fluctuate strongly, the number of channels nevertheless increase monotonically with increasing gate voltage, agreeing with the intuition of gate-tuning the number of occupied electron states in the junction. This regime is also characterized by random scatters of CPR amplitude vs. skew, with little correlation.

Above $V_C \approx -0.45$ V, additional channels enter with transmission coefficients approaching unity rapidly with gate voltage. This regime is characterized by consistently forward-skewed CPR (S ~ 0.3) and monotonically increasing critical current amplitude with gate voltage.

USING NUMERICAL SIMULATIONS TO STUDY THE INTERPLAY OF ELECTROSTATIC POTENTIAL, SPATIAL STRUCTURE, AND SPECTRUM OF ANDREEV STATES

Although the short junction model provides an intuitive description of the number and transparency of modes in the junction, it is limited in its ability to faithfully represent device behavior. In a real device, the spectrum and spatial distribution of states will be influenced by the device geometry, material composition, and details of the electrostatic potential [35–37]. Understanding these effects is important for device engineering in qubit and Majorana applications, motivating a more detailed model of the observed CPR.

We study a microscopic model of the system, consisting of two wires and a junction, the geometry shown in the figure 3a. The wire's state is controlled by three electric gates: two below the wires and the cutter gate in the junction. In the normal state it is described by the following low-energy Hamiltonian

$$\hat{H}_n = \frac{1}{2m^*} \left(\hat{k}_x^2 + \hat{k}_y^2 + \hat{k}_z^2 \right) + V(x,z) - \alpha \left(\hat{k}_x \sigma_y - \hat{k}_y \sigma_x \right),$$
(3)

where operators $\hat{k}_{x,y,z}$ denote the momentum in x, y, z directions, $\sigma_{x,y,z}$ are Pauli matrices, $m^* = 0.026$ m_e [1] is the effective mass in InAs (m_e being the electron mass), $\alpha = 0.01$ eV·nm is the spin-orbit coupling [1] and V is the electrostatic potential, created by the electric gates. The potential is translationally invariant along the y direction and can be calculated solving the Poisson equation $\nabla^2 V(x,z) = -\frac{en(x,z)}{\varepsilon_0 \varepsilon_r}$ with $\varepsilon_r = 15.2$ and the boundary conditions set by the voltages of the surrounding gates and the band-offset at the interface of InAs and Al, which we take as $W = 0.25$ eV. Boundary conditions between the wire and vacuum in the junction region are set to zero to model a well with a resonant character of current transmission through the junction, as observed in figure 2e. In order to obtain the potential one has to self-consistently determine density of electrons and the potential in a Schrodinger-Poisson loop, which is computationally prohibitive. Instead we employ the Thomas-Fermi approximation for the density $n = \frac{1}{3\pi^2} \left(\frac{2m^* \phi}{\hbar^2} \right)^{\frac{3}{2}}$, which produces excellent agreement for the potential with the full Schrodinger-Poisson method [35, 38].

Superconductivity is included using a Bogoliubov-de-Gennes Hamiltonian and adding pairing potentials Δ and $\Delta e^{i\phi}$ to the left and right proximitized segments of the wires respectively, leading to the phase difference ϕ across the junction. The numerical complexity is alleviated by projecting the Hamiltonian in the y direction to the basis of sinusoidal eigenstates [35, 39].

The zero-temperature CPR is calculated from the Andreev spectrum by taking the derivative of the ground state energy with respect to ϕ (see Eq. (1)) [40]. The gate dependence of the simulated critical current is shown in the upper panel of figure 3c) (black), and is qualitatively similar to the experimental data. As the gate voltage increases, an insulating regime transitions into three well-separated peaks, which then evolve into a regime of fluctuating critical current. Within the regime of recurring peaks, the simulated supercurrent is dominated by the contribution from a single mode. The well-separated peaks in the Josephson current is indicative of tunneling through resonant levels in the junction [25]. The skew of the modeled CPR tends to increase and decrease with the critical current (light blue in figure 3c). Plot-

a. Model geometry & electrostatic potential

b. Density of states

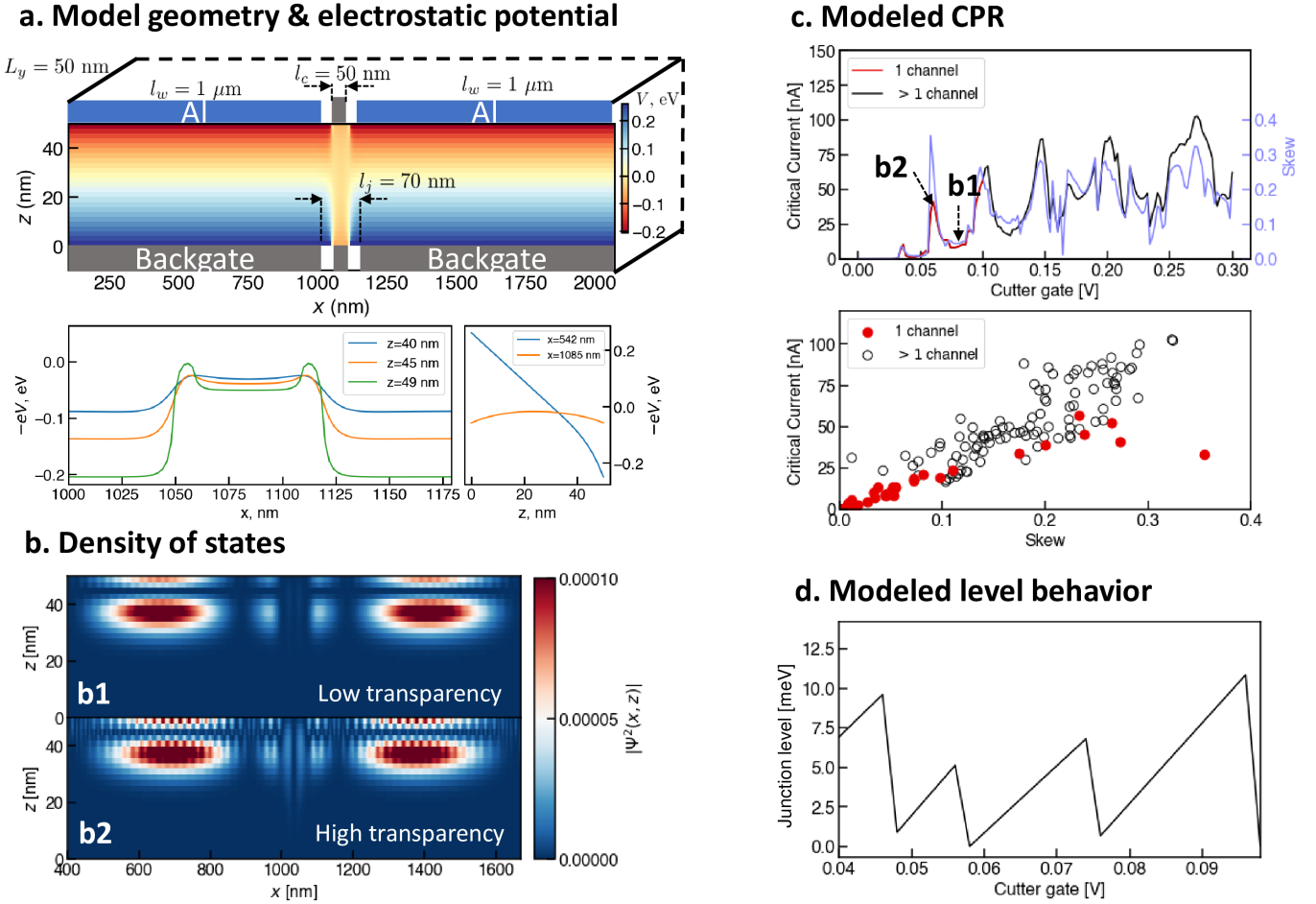## c. Modeled CPR

d. Modeled level behavior

FIG. 3. Numerical simulations of the InAs junction. a) Top: schematics of the simulated model, consisting of two wire segments and the junction, each augmented with an electric gate. Empty spaces at the interface of the wire and vacuum in the junction indicate zero boundary value of potential. Color indicates the calculated electrostatic potential for the left/right gate voltage −0.29 V and cutter voltage 0.06 V. Bottom panel: 2d cuts of the electrostatic potential along the x direction (left) and along the z direction (right). b) The density of the lowest positive Andreev state at phase $\phi = \pi$ in the junction at cutter voltage 0.07V (top, b1) and 0.06V (bottom, b2), corresponding to the regimes of low and high transparency in the junction respectively. Color scale shows the probability density calculated as the square of the wave function amplitude. c) Top: Calculated dependence of the critical current (red/black) and skew (blue) on the cutter gate voltage. Arrows indicate the gate voltages of b1, b2 plots. Bottom: The dependence of the calculated critical current on the skew. In both panels red color indicates the single-channel regime. d) The dependence of the position of the highest occupied level in the junction on the cutter gate voltage.

ting the simulated skews and critical currents against one another reveals that this relationship strongly resembles the experiment (lower panel in figure 3c). The simulated behavior with only one contributing mode, plotted in red, shows strong correlation between critical current and skew. These single-channel points lie predominantly along the bottom part of the scatter plot, as found experimentally.

The excellent agreement between the measured and simulated CPRs provides an opportunity to further examine the electronic structure of the device. In figure 3b, the local density of states in the single-channel regime reveals a striking difference in the structure of low and high transparency states (also indicated by black arrows in figure 3c). In both cases the band offset between alu-

minum and InAs leads to an enhanced density of states in the nanowire near the aluminum coating. At high transparency ($\tau \approx 0.98$), the density of states becomes much larger in the junction than that at low transparency ($\tau \approx 0.32$). The change between regimes occurs in the range of 10 mV difference in V_C, indicating the delicate nature of the quantum states in the junctions formed by InAs nanowires.

Figure 3d shows the evolution with cutter gate voltage of highest occupied level energy in the junction, where zero energy corresponds to the chemical potential of the leads. This simulation demonstrates that sweeping the cutter gate voltage can be expected to bring a series of states in and out of resonance with the leads. In particular, the vertical jumps indicate that the resonant-level

spacings (ΔE) are of order a few meV. This $\Delta E \gg \Delta_{SC}$ (where Δ_{SC} is the superconducting gap of the leads) gives rise to multiple resonance peaks in the single-channel regime. As further proof of resonant tunneling behavior, the level energy minima near $V_C = 0.058$ V and $V_C = 0.1$ V coincide with the Fermi energy of the leads ($E = 0$), and at the same time correspond precisely to the first two supercurrent peaks in figure 3c. All other energies in panel d are far from $E = 0$ and correspond to suppressed supercurrent in panel c.

INTERACTING BEHAVIOR IN THE SINGLE-MODE PEAKED REGIME

We now focus on the single-channel regime, to investigate in more detail the series of recurring peaks in critical current (figure 4a). When the cutter gate voltage V_C is tuned away from the peaks, the CPR is consistent with non-interacting short junction theory. Near two of these peaks, however, the CPR deviates from the non-interacting behavior and instead displays a shoulder near phase $\phi = \pi$ (figure 4b). The shoulder features are a precursor to π-junction behavior resulting from Coulomb blockade effect[41–49], and have been studied experimentally in a carbon nanotube Josephson junction [50]. Related phenomena have also been observed in nanowire-superconductor hybrids [17, 51–54], but without quantitative modeling of the CPR.

To understand the shoulder behavior in the CPR, we consider a scenario where a quantum dot (QD) is formed in the junction. The QD is characterized by the strength of the local Coulomb electron-electron interaction U and a single spin-degenerate level with energy ξ measured relative to the chemical potential of the leads (see figure 4c). Coupling strengths to the right/left leads $\Gamma_{R/L}$ and the energy ξ depend on the cutter gate voltage. Following Ref. [43] we treat interactions within the mean-field approximation and introduce a local exchange field $J = U(\langle n_\downarrow \rangle - \langle n_\uparrow \rangle)/2$ where $\langle n_{\uparrow/\downarrow} \rangle$ are single-level occupation probabilities for spin-up and spin-down electrons. In the limit when $\Gamma_R = \Gamma_L = \Gamma \gg \Delta$, the resulting Andreev energies can be obtained analytically:

$$\epsilon_\pm = \Delta \sqrt{\frac{\cos^2 \phi/2 + 2E^2 + Z^2(Z^2 + \sin^2 \phi/2) \pm 2XS(\phi)}{Z^4 + 2(X^2 + E^2) + 1}}.$$
(4)

Here ϕ is the phase difference $\phi_L - \phi_R$ between the left and right leads, $S(\phi) = \sqrt{Z^2 \cos^2 \phi/2 + E^2 + (\sin^2 \phi)/4}$, $E = \xi/2\Gamma$, $X = J/2\Gamma$, and $Z^2 = X^2 - E^2$. With the above formula for the Andreev spectrum, we have the following expression for the current-phase relation:

$$I(\phi) = -\frac{e}{\hbar} \left(\tanh \left(\frac{\epsilon_+}{2k_B T} \right) \frac{d\epsilon_+}{d\phi} + \tanh \left(\frac{\epsilon_-}{2k_B T} \right) \frac{d\epsilon_-}{d\phi} \right).$$
(5)

In this model, the expected junction behavior results from an interplay between the level energy ξ and the on-site exchange coupling J. The characteristics peaks in the supercurrent observed in the experiment, see figure 4a, are related to the charge-degeneracy points. We now analyze CPR using a simple model above and consider $\xi/\Gamma = 0$ case. Without interactions, such a situation corresponds to a resonant transmission through the QD with CPR given by the red line in figure 4d. The exchange interactions effectively split spin-degenerate level, creating level crossings away from $\phi = \pi$ (black curves in figure 4d). Using this spectrum one finds the appearance of a shoulder near $\phi = \pi$ in CPR. Larger interaction strength leads to level crossings farther away from $\phi = \pi$, thus wider shoulders in CPR. By fitting the experimental data to the Eq. (5), we find a good agreement with the measured CPR data, with best fit values for the interaction strength given by $J/\Gamma = 0.39$ and 0.42 when $V_C = -1.54$ V and -1.79 V respectively (red dashed curve in figure 4b is the best fit).

Away from the single-particle resonance (i.e. $\xi \neq 0$), the dispersion of the Andreev states with ϕ gets suppressed due to the reduction in transmission probability through the QD. A nonzero exchange energy splits the Andreev level spin-degeneracy as before, but as long as $\xi \gg J$ the levels will not cross at zero energy. Thus, one expects the reversal of the supercurrent to appear in the CPR only when the junction is tuned near resonance. Indeed, we only observe shoulders in the CPR near peaks in the critical current, consistent with the theoretical predictions.

Fitting the measured CPR to Eq. (5) throughout the single-channel regime allows one to extract the cutter gate dependence of the normalized site energy, ξ/Γ (figure 4f). As the cutter gate increases from -2 V to -1.16 V, three levels are tuned in and out of resonance with the leads. In addition to shifting the spectrum, the cutter gate is expected to modify the shape of the confining potential in the junction and the coupling Γ. We speculate that the coupling Γ may increase with V_C, contributing to the decrease in slopes in figure 4f as V_C becomes more positive. The experimentally extracted evolution of levels agrees qualitatively with numerical simulations (see figure 3d).

In the measurements discussed so far, only the cutter gate voltage was varied, with all other gates grounded. With negative voltage V_S applied to the two side gates, we observed additional CPRs with shoulder-like features. Fitting these CPRs to Eq. (5) yielded values for the normalized exchange energy J/Γ. As the side gate voltages become more negative, we find an increase in the mean value of J/Γ at each gate voltage (figure 4g and [28]). Fringe electric fields at the two ends of the junction may lead to decreased coupling Γ with more negative V_S, con-

a. Peaked structure in the single-channel regime

b. CPR reveals finite charging energy

c. Modeling CPR with charging energy

d. Modeled Andreev Spectrum

f. Using cutter gate to tune ξ/Γ

e. Modeled CPR

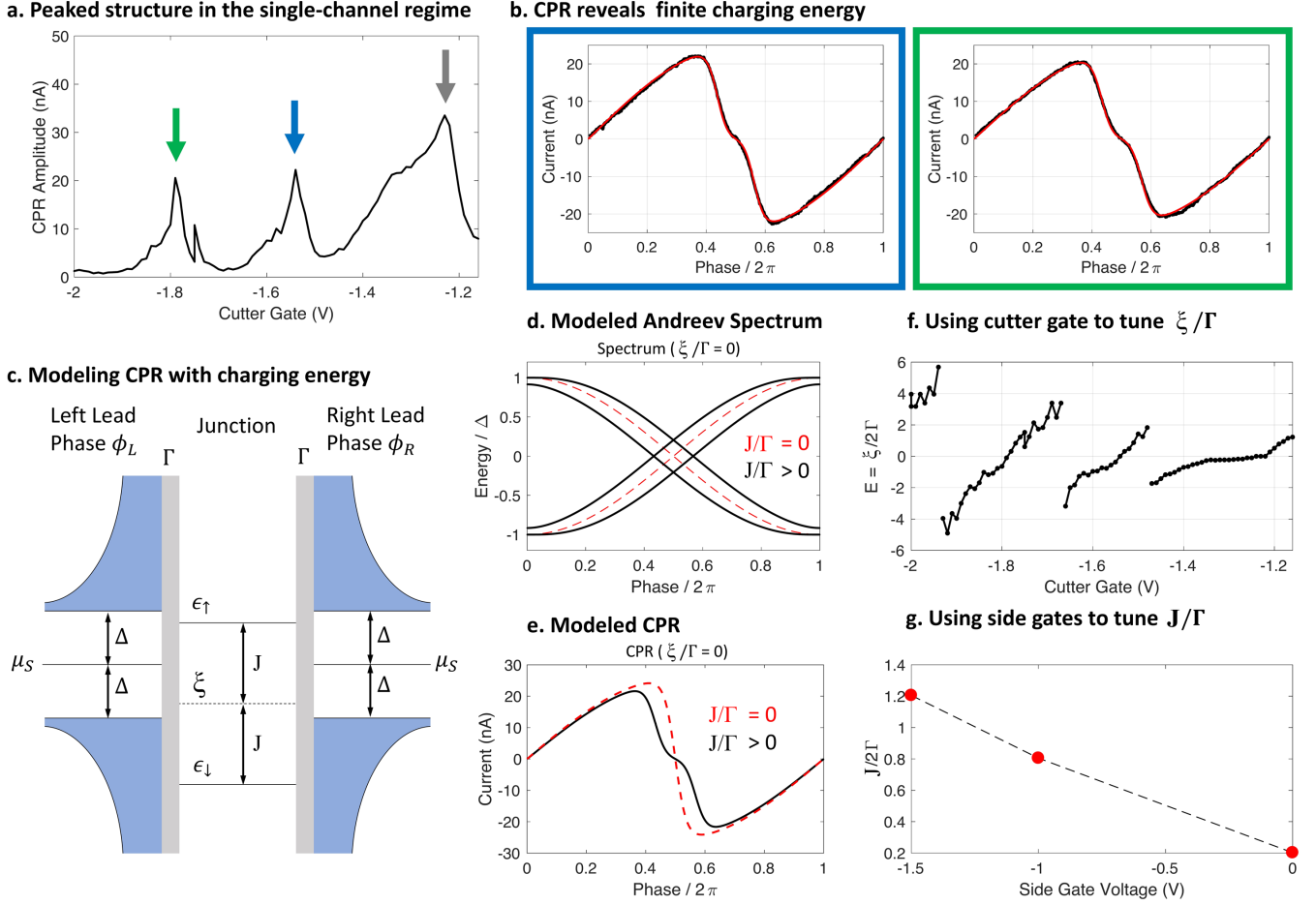**g. Using side gates to tune J/Γ**

FIG. 4. Using the CPR to elucidate the role of interactions in the single-channel regime. a) In the single-channel regime, the CPR amplitude develops recurring peaks, indicated by arrows. b) At two of these peaks, a shoulder appears in the CPR near phases equal to π modulo 2π. The colored borders surrounding the plots correspond to colored arrows in (a). The appearance of the shoulders in the CPR is evidence for finite charging energy in the junction region of the device. c) Modeling our device with finite charging energy allows calculation of CPRs in this regime. The two leads, with gap Δ and chemical potential μ_s, are coupled to the junction symmetrically with coupling Γ. The charging energy is modeled as an exchange energy J in the device, which splits a state at energy ξ in the junction into an odd and even parity state with respective energies $\epsilon_\downarrow$ and $\epsilon_\uparrow$. d, e) The model allows calculation of the spectrum of Andreev states and the CPR, shown here without charging energy (red dashed), and with finite charging energy (black). The appearance of a shoulder is characteristic of finite charging energy when $\xi/\Gamma \approx 0$, and can be used in fits to the data (red curves in (b)). f) Fitting the model to the data throughout the single-channel regime reveals the evolution of energy levels in the device. g) The model can also be fit to the data at different values of side gate voltage, revealing that more negative side gate voltage corresponds to increased J/Γ.

sistent with this finding. We observed no shoulder-like features in any CPR with positive side gate voltage.

DISCUSSION

Our fits to the current-phase relationship in figure 2 indicate the amplitude of Andreev bound states of $\Delta = 128$ μeV, which is smaller than the proximity-induced gap for similar devices [12]. Unlike conventional metallic Josephson junctions, where a normal region is sandwiched between two superconducting leads, our junction is formed by two semiconducting wire segments with proximity-

induced gap and contains an emergent resonant level. Therefore, the scattering processes that lead to the Andreev bound states involve both normal scattering from the resonant level in the junction to the semiconducting wire segments, and Andreev reflections at the interface with the superconductor. The Andreev spectrum here is closely related to that of a resonant level coupled to two superconductors, and the amplitude of the Andreev states in this scenario depends on the coupling of the dot to the wires [55].

In the absence of a Zeeman field, spin-orbit coupling gives a small correction to the Andreev spectrum [56, 57]. Spin-orbit-induced corrections to two energy levels re-

lated by time-reversal symmetry have opposite signs. Since the total Josephson current is a summation over all time-reversed pairs of ABS, spin-orbit-induced corrections to the supercurrent are small. The main effect of spin-orbit coupling here is actually a modification to the Fermi momenta mismatch that affects normal reflection [56], thus largely indistinguishable from a small change in the Josephson junction transmission coefficient in the short-junction model.

In comparison to Ref. [17], the present work focuses on a narrower range of negative gate voltage corresponding to the few-mode regime. In this regime, we observed qualitatively similar resonant peaks followed by CPR amplitude and shape fluctuations, as the number of supercurrent-carrying modes increases from one to several. Such features are not universal, but depend on the geometry-induced electrostatic environment, as evidenced by our numerical modeling. The nanowire in Ref. [17] had 6-facets Al shell and a global Au bottom gate, whereas the nanowire in this work has 4-facets Al shell and a wrap-around finger gate. As a result, the gate dependence of the mode structure is expected to differ quantitatively, as observed. Common to both works, as more modes are added to the junction, the CPR becomes consistently forward skewed (S $\sim$ 0.2 in Ref. [17] and S $\sim$ 0.3 in the present work).

The analysis of the effect of Coulomb interaction, evident from the appearance of a "shoulder" at phase $= \pi$, is consistent with the observation of "backward skewness" in Ref. [17]. When side gates are tuned to -1.5 V, the CPR evolves into a "backward skewed" shape, where the maximum occurs at a phase $< \frac{\pi}{2}$ (figure S3 in [28]). The dot behavior in the present device is emergent and not gate defined. Due to the location of the side gates and screening from the epitaxial Al shell, we are unable to independently control tunnel barriers and position of energy levels on the dot. To achieve full supercurrent reversal (as demonstrated in Ref. [53]), one needs to tune the system into strong Coulomb-blockade regime, which is difficult to do in our system.

CONCLUSION

Our measurements and analysis distinguish between a multi-channel regime and a single-channel regime with widely tunable anharmonicity and interactions. Our CPR-based technique for comparing experiment and numerical simulations allows detailed study of the interplay between mode structure and electrostatics, and may be extended to the design and analysis of future superconductor-semiconductor heterostructures [58].

The propensity for quantum dot formation in a nanowire-based junction, even in the absence of tunnel barrier gates, may be related to the electrostatic potential induced by the Al shell, thus must be carefully considered for Majorana measurements on superconductor-nanowire hybrids.

The presence of interactions at low electron density also has implications for experiments examining mode behavior in superconductor-nanowire hybrids, where interactions are sometimes neglected. For example, a recent work examined multiple Andreev reflections as a probe of transparency in few-mode junctions, but ignored interaction effects which are known to influence IV characteristics [18, 59]. Spectroscopy experiments also studied anharmonicity and Zeeman-induced spin-splitting of Andreev levels in the few-mode regime, but may also be affected by splitting effects from interactions as examined in our work [16, 19]. Overall our ability to accurately model device behavior, as well as to understand and control both interactions and anharmonicity, will elucidate the interpretation of current experiments and provide a method for device design.

[1] R. Lutchyn, E. Bakkers, L. Kouwenhoven, P. Krogstrup, C. Marcus, and Y. Oreg, Nature Review Materials **3**, 52 (2018).

[2] A. Y. Kitaev, Physics-Uspekhi **44**, 131 (2001).

[3] R. M. Lutchyn, J. D. Sau, and S. Das Sarma, Phys. Rev. Lett. **105**, 077001 (2010).

[4] Y. Oreg, G. Refael, and F. von Oppen, Phys. Rev. Lett. **105**, 177002 (2010).

[5] V. Mourik, K. Zuo, S. M. Frolov, S. R. Plissard, E. P. A. M. Bakkers, and L. P. Kouwenhoven, Science **336**, 1003 (2012).

[6] M. Deng, C. Yu, G. Huang, M. Larsson, P. Caroff, and H. Xu, Nano Letters **12**, 6414 (2012).

[7] A. Das, Y. Ronen, Y. Most, Y. Oreg, M. Heiblum, and H. Shtrikman, Nature Physics **8**, 887 (2012).

[8] L. P. Rokhinson, X. Liu, and J. K. Furdyna, Nature Physics **8**, 795 (2012).

[9] H. O. H. Churchill, V. Fatemi, K. Grove-Rasmussen, M. T. Deng, P. Caroff, H. Q. Xu, and C. M. Marcus, Phys. Rev. B **87**, 241401 (2013).

[10] A. D. K. Finck, D. J. Van Harlingen, P. K. Mohseni, K. Jung, and X. Li, Phys. Rev. Lett. **110**, 126406 (2013).

[11] S. M. Albrecht, A. P. Higginbotham, M. Madsen, F. Kuemmeth, T. S. Jespersen, J. Nygård, P. Krogstrup, and C. M. Marcus, Nature **531**, 206 (2016).

[12] M. T. Deng, S. Vaitiekenas, E. B. Hansen, J. Danon, M. Leijnse, K. Flensberg, J. Nygård, P. Krogstrup, and C. M. Marcus, Science **354**, 1557 (2016).

[13] H. Zhang, C.-X. Liu, S. Gazibegovic, D. Xu, J. A. Logan, G. Wang, N. van Loo, J. D. S. Bommer, M. W. A. de Moor, D. Car, R. L. M. Op het Veld, P. J. van Veldhoven, S. Koelling, M. A. Verheijen, M. Pendharkar, D. J. Pennachio, B. Shojaei, J. S. Lee, C. J. Palmstrøm, E. P. A. M. Bakkers, S. D. Sarma, and L. P. Kouwenhoven, Nature **556**, 74 (2018).

[14] T. W. Larsen, K. D. Petersson, F. Kuemmeth, T. S.

Jespersen, P. Krogstrup, J. Nygård, and C. M. Marcus, Phys. Rev. Lett. **115**, 127001 (2015).

[15] G. de Lange, B. van Heck, A. Bruno, D. J. van Woerkom, A. Geresdi, S. R. Plissard, E. P. A. M. Bakkers, A. R. Akhmerov, and L. DiCarlo, Phys. Rev. Lett. **115**, 127002 (2015).

[16] D. van Woerkom, A. Proutski, B. van Heck, D. Bouman, J. Väyrynen, L. Glazman, P. Krogstrup, J. Nygård, L. Kouwenhoven, and A. Geresdi, Nature Physics **13**, 876 (2017).

[17] E. Spanton, M. Deng, S. Vaitiekėnas, P. Krogstrup, J. Nygård, C. Marcus, and K. Moler, Nature Physics **13**, 1177 (2017).

[18] M. Goffman, C. Urbina, H. Pothier, J. Nygård, C. Marcus, and P. Krogstrup, New Journal of Physics **19**, 092002 (2017).

[19] A. Kringhøj, L. Casparis, M. Hell, T. W. Larsen, F. Kuemmeth, M. Leijnse, K. Flensberg, P. Krogstrup, J. Nygård, K. D. Petersson, and C. M. Marcus, Phys. Rev. B **97**, 060508 (2018).

[20] M. Hays, G. de Lange, K. Serniak, D. J. van Woerkom, D. Bouman, P. Krogstrup, J. Nygård, A. Geresdi, and M. H. Devoret, Phys. Rev. Lett. **121**, 047001 (2018).

[21] L. Tosi, C. Metzger, M. F. Goffman, C. Urbina, H. Pothier, S. Park, A. L. Yeyati, J. Nygård, and P. Krogstrup, Phys. Rev. X **9**, 011010 (2019).

[22] C. D. English, D. R. Hamilton, C. Chialvo, I. C. Moraru, N. Mason, and D. J. Van Harlingen, Phys. Rev. B **94**, 115435 (2016).

[23] I. Sochnikov, A. J. Bestwick, J. R. Williams, T. M. Lippman, I. R. Fisher, D. Goldhaber-Gordon, J. R. Kirtley, and K. A. Moler, Nano Letters **13**, 3086 (2013).

[24] I. Sochnikov, L. Maier, C. A. Watson, J. R. Kirtley, C. Gould, G. Tkachov, E. M. Hankiewicz, C. Brüne, H. Buhmann, L. W. Molenkamp, and K. A. Moler, Phys. Rev. Lett. **114**, 066801 (2015).

[25] C. W. J. Beenakker, Phys. Rev. Lett. **67**, 3836 (1991).

[26] J. R. Kirtley, L. Paulius, A. J. Rosenberg, J. C. Palmstrom, C. M. Holland, E. M. Spanton, C. L. Jermain, J. Gibbons, Y.-K.-K. Fung, M. E. Huber, D. C. Ralph, M. B. Ketchen, G. W. Gibson Jr., and K. A. Moler, Review of Scientific Instruments **87**, 093702 (2016).

[27] L. D. Jackel, R. A. Buhrman, and W. W. Webb, Phys. Rev. B **10**, 2782 (1974).

[28] See Supplemental Material at [URL by publisher] for more discussion on gating, experimental uncertainty and model fitting procedure [12, 17, 23, 24, 26, 35, 60–63].

[29] P. Krogstrup, N. L. B. Ziino, W. Chang, S. M. Albrecht, M. H. Madsen, E. Johnson, J. Nygård, C. M. Marcus, and T. S. Jespersen, Nature Materials **14**, 400 (2015).

[30] C. W. J. Beenakker and H. van Houten, in *Proceedings of the International Symposium on Nanostructures and Mesoscopic Systems* (Academic Press, Inc., 1992) pp. 481–497.

[31] I. Kulik and A. Omelyanchuk, Zh. Eksp. Teor. Fiz. Piz. Red. **21**, 216 (1975).

[32] W. Haberkorn, H. Knauer, and J. Richter, Physica Status Solidi (a) **47**, K161 (1978).

[33] A. Zaĭtsev, Zh. Eksp. Teor. Fiz. Piz. Red. **86**, 1742 (1984).

[34] H. Bluhm and K. A. Moler, Review of Scientific Instruments **79**, 014703 (2008), https://doi.org/10.1063/1.2835716.

[35] A. E. Antipov, A. Bargerbos, G. W. Winkler, B. Bauer, E. Rossi, and R. M. Lutchyn, Phys. Rev. X **8**, 031041 (2018).

[36] B. D. Woods, T. D. Stanescu, and S. Das Sarma, Phys. Rev. B **98**, 035428 (2018).

[37] G. W. Winkler, A. E. Antipov, B. van Heck, A. A. Soluyanov, L. I. Glazman, M. Wimmer, and R. M. Lutchyn, ArXiv e-prints (2018), arXiv:1810.04180 [cond-mat.supr-con].

[38] A. E. G. Mikkelsen, P. Kotetes, P. Krogstrup, and K. Flensberg, Phys. Rev. X **8**, 031040 (2018).

[39] T. D. Stanescu, R. M. Lutchyn, and S. Das Sarma, Phys. Rev. B **84**, 144522 (2011).

[40] M. Cheng and R. M. Lutchyn, Phys. Rev. B **86**, 134522 (2012).

[41] B. I. Spivak and S. A. Kivelson, Phys. Rev. B **43**, 3740 (1991).

[42] A. V. Rozhkov and D. P. Arovas, Phys. Rev. Lett. **82**, 2788 (1999).

[43] E. Vecino, A. Martín-Rodero, and A. L. Yeyati, Phys. Rev. B **68**, 035105 (2003).

[44] F. Siano and R. Egger, Phys. Rev. Lett. **93**, 047002 (2004).

[45] M.-S. Choi, M. Lee, K. Kang, and W. Belzig, Phys. Rev. B **70**, 020502 (2004).

[46] G. Sellier, T. Kopp, J. Kroha, and Y. S. Barash, Phys. Rev. B **72**, 174502 (2005).

[47] C. Karrasch, A. Oguri, and V. Meden, Phys. Rev. B **77**, 024517 (2008).

[48] T. Meng, S. Florens, and P. Simon, Phys. Rev. B **79**, 224521 (2009).

[49] G. Kiršanskas, M. Goldstein, K. Flensberg, L. I. Glazman, and J. Paaske, Phys. Rev. B **92**, 235422 (2015).

[50] R. Delagrange, D. J. Luitz, R. Weil, A. Kasumov, V. Meden, H. Bouchiat, and R. Deblock, Phys. Rev. B **91**, 241401 (2015).

[51] W. Chang, V. E. Manucharyan, T. S. Jespersen, J. Nygård, and C. M. Marcus, Phys. Rev. Lett. **110**, 217005 (2013).

[52] E. Lee, X. Jiang, M. Houzet, R. Aguado, C. Lieber, and S. De Franceschi, Nature Nanotechnology **9**, 79 (2014).

[53] J. van Dam, Y. Nazarov, E. Bakkers, S. De Franceschi, and L. Kouwenhoven, Nature **442**, 667 (2006).

[54] D. B. Szombati, S. Nadj-Perge, D. Car, S. R. Plissard, E. P. A. M. Bakkers, and L. P. Kouwenhoven, Nature Physics **12**, 568 (2016).

[55] C. W. J. Beenakker, arXiv e-prints , cond-mat/0406127 (2004), arXiv:cond-mat/0406127 [cond-mat.mes-hall].

[56] M. Cheng and R. M. Lutchyn, Phys. Rev. B **86**, 134522 (2012).

[57] B. Bri, J. H. Bardarson, and C. W. J. Beenakker, Physical Review B **77**, 045311 (2008).

[58] S. Vaitiekėnas, A. M. Whiticar, M.-T. Deng, F. Krizek, J. E. Sestoft, C. J. Palmstrøm, S. Marti-Sanchez, J. Arbiol, P. Krogstrup, L. Casparis, and C. M. Marcus, Phys. Rev. Lett. **121**, 147701 (2018).

[59] Y. Avishai, A. Golub, and A. Zaikin, Europhysics Letters **54**, 5 (2001).

[60] S. Vaitiekėnas, M.-T. Deng, J. Nygård, P. Krogstrup, and C. M. Marcus, Phys. Rev. Lett. **121**, 037703 (2018).

[61] P. Bevington and D. Robinson, *Data Reduction and Error Analysis for the Physical Sciences*, McGraw-Hill Higher Education (McGraw-Hill Education, 2003).

[62] E. B. Rosa and F. W. Grover, *Formulas and Tables for the*

Calculation of Mutual and Self Inductance. (Revised.), Vol. 1(1/2) (The Washington Academy of Sciences, 1911) p. 1416.

[63] E. H. Brandt, Phys. Rev. B **72**, 024529 (2005).

ACKNOWLEDGEMENT